H-matrix accelerated FEM-BEM coupling for dynamic analysis of naval structures in pulsating potential fluids

Damien Mavaleix-Marchessoux, Marc Bonnet, Stéphanie Chaillat, Bruno Leblé

$\mathcal{H}$-matrix accelerated BEM-FEM coupling for dynamic analysis of naval structures under pulsating potential flow motion

Damien Mavaleix-Marchessoux[1,2], Marc Bonnet[1], Stéphanie Chaillat[1], and Bruno Leblé[2]

[1]*POEMS (CNRS-ENSTA-INRIA), ENSTA Paris - Institut Polytechnique de Paris, 828 Bd des Maréchaux, 91120 Palaiseau Cedex, FRANCE*

[2]*Naval Group Research, Technocampus Ocean, 5 Rue de L'Halbrane, 44340 Bouguenais, FRANCE*

Abstract

This article addresses one of the components of our ongoing work towards an efficient computational modeling methodology for evaluating all effects on a submerged structure of a remote underwater explosion. Following up on a previous study devoted to computing the transient acoustic fields induced by the shock wave initially sent by the blast on a rigid submarine, we focus here on the second stage of the underwater event, namely solving the transient fluid-structure interaction (FSI) between the structure and the incompressible potential flow induced by the delayed, and slower, oscillations of the gas bubble created by the remote blast.

The boundary element method (BEM) is the best-suited approach for handling potential flow problems in large fluid domains (idealized as unbounded), whereas the finite element method (FEM) naturally applies to the transient structure analyses. To perform the FEM-BEM coupling we use a sub-cycling approach that alternates fluid and solid analyses with Neumann boundary conditions. The transient nature of the coupled analysis and the recourse to sub-cycling together make the overall procedure rely on a large number of BEM potential flow solutions, while the complexities of the wet surface and of the solid transient response imply a need for large BE models for the flow potential. This combination of reasons mandates accelerating the BE component.

Accordingly, our main contribution is to study the feasibility and effectiveness of coupling the Hierarchical-matrix accelerated BEM ($\mathcal{H}$-BEM) and the FEM for the FSI problems of interest. In particular, we show that the same integral operators can be used at all time instants in spite of the expected global motion of the submerged structure, a feature that the $\mathcal{H}$-BEM can exploit to full advantage. The proposed original treatment is validated against analytical solutions for the case of a motionless or mobile rigid spherical immersed object, and then tested on a complex configuration representative of target applications.

Keywords:. FEM-BEM coupling; Fluid-structure interaction; Fast BEM; Underwater explosion

1 Introduction

Submarines must be designed to withstand the effects of underwater explosions (see Fig. 1). Given the very high cost of full-scale experimental testing, assessing the effects of a remote underwater explosion on a given structure rests largely on numerical simulation methods. An underwater explosion is a complex event [10, 31] that unfolds in two stages having quite different time scales. In the first (fast) stage, a shock wave is sent, and its effects can be modelled near the structure using a linear acoustic model for the fluid. In the second stage, the hot gases resulting from the explosion form a pulsating bubble, inducing a slower and delayed fluid motion that can be treated as an incompressible potential flow. The blast is assumed to be sufficiently remote for the two phenomena as experienced by the ship to be temporally separated.

Our overall goal is to develop a computational methodology for the fluid-structure interaction (FSI) problem taking into account all effects of the remote blast. A previous study [27] investigated the computation of transient acoustic fields induced by the shock wave of the blast on a rigid submarine. In this work, we focus on the second stage, i.e. the transient FSI between the submarine and the incompressible potential flow induced by the oscillating bubble of gas. The water domain (the ocean) is assumed to be unbounded, i.e., the free surface (water surface) and the seabed are disregarded. The water is treated as a homogeneous and inviscid fluid experiencing irrotational flows.

Domain discretisation methods such as the FEM are viable approaches for the treatment of incompressible potential flow. However, the boundary element method (BEM) [7], based on the discretisation of boundary integral equations (BIEs), is very well suited to the present situation involving potential flow problems in large fluid domains (idealized as unbounded), as it only requires the discretisation of the submarine wet surface, whose size and geometrical details may lead to meshing difficulties with domain discretization. The BEM is indeed used for the present type of applications in e.g. [24, 35–37].

The perturbation induced by the bubble of an underwater explosion, and the correlated FSI problem with a structure, have been extensively studied in the literature [2, 4, 12–14, 17, 32, 38]. In particular, bubble models with varying degrees of complexity, describing the bubble dynamics and the induced fluid motion in the absence of a submerged structure, have been proposed [14, 23]. In this work, the submarine is assumed to remain far enough from the bubble during the whole analysis, so that the bubble dynamics is only marginally affected by its presence. Based on this hypothesis, the FSI problem is then formulated in terms of coupling a potential flow and the dynamical response of the structure, using an existing bubble model (and especially the velocity potential describing the ambient flow) as input; in practice we rely on the in-house bubble dynamic simulation proposed in [23].

The specific industrial context of this work moreover dictates that the transient structure analyses be effected using the dedicated FE platform Abaqus ®, which is not open-source and sets limitations on the implementation of BE-FE coupling procedures. In particular, non-homogeneous Robin boundary conditions, upon which iterative domain decomposition methods with guaranteed convergence are often based, are not available in this framework (see [26], Sec. 3.2.2). We thus resort to a sub-cycling approach that alternates fluid and solid analyses with Neumann boundary conditions. The transient nature of the overall coupled analysis and the recourse to sub-cycling together make the overall procedure rely on a large number M of BEM potential flow solutions, while the complexity of the wet surface and of the solid transient response imply a need for models featuring large numbers N of BE unknowns for the flow potential; we expect applications to require $M \sim 10^3 - 10^4$ and $N \sim 10^4 - 10^5$. This combination of reasons mandates accelerating the BE component. We show that under reasonable assumptions all BE solutions can be obtained by re-using the same time-independent governing integral operators in spite of the expected global motion of the submerged structure. This makes the $\mathcal{H}$-matrix compression method a natural acceleration method, whereby blockwise data-sparse low-rank approximations of the relevant integral operators are pre-computed and stored, then used for accelerating the matrix-vector products incurred in the GMRES iterations yielding all subsequent BE solutions.

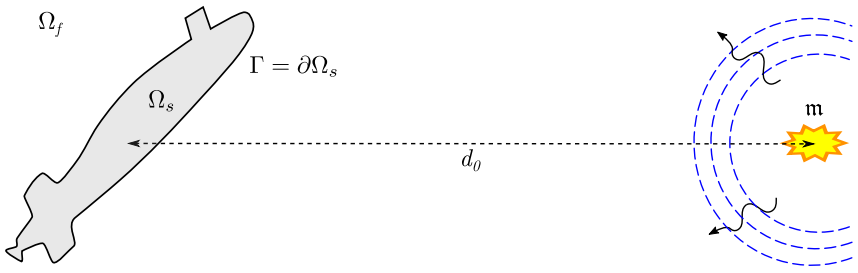

Figure 1: *Submarine experiencing a remote underwater blast.*

The main goal of this work is to show the feasibility and effectiveness of coupling the $\mathcal{H}$-matrix accelerated BEM and the FEM, and taking full advantage of the established reusability of integral operators in this context, for analysing the transient effect of water motions induced by the pulsating bubble effect on submerged structures. The article is organised as follows. The governing equations for our FSI problem and their underlying physical and computational hypotheses, are given in Section 2, together with the main ingredients for the iterative BEM-FEM coupling solution method. The accelerated BEM for the fluid domain is then presented in Section 3, with emphasis on the reasons allowing the reusability of integral operators. The proposed treatment is validated in Section 4 against analytical solutions for the case of a motionless or mobile rigid spherical object. Finally, a complex configuration representative of target applications is treated in Section 5.

2 FSI problem: hypotheses and formulation

2.1 Hypotheses and modeling. The bubble motion is assumed to be slow enough for the fluid to be treated as incompressible, irrotational and non-viscous. Under these assumptions, the fluid velocity derives from a velocity potential ϕ that is a harmonic function, and the fluid pressure is inferred through Bernoulli's equation (see (3b) below). We assume the knowledge of a bubble model, that is, a time-dependent velocity potential ϕ^{amb} (called ambient potential in the sequel) that describes the fluid motion created by a pulsating bubble in the surrounding fluid medium in the absence of a submerged structure. The ambient potential depends on time-dependent parameters describing the bubble motion itself, which are governed by ODEs resulting from energy conservation considerations. In practice, we use in this work the Hicks bubble model [20, 23] to describe the bubble dynamics in the absence of the ship; in this model, whose details are recalled in Section 5.2, the bubble is assumed to remain spherical while vertically moving upwards (Fig. 2), and $\phi^{\text{amb}}(\mathbf{x}, t)$ depends on the bubble radius $R(t)$ and depth $Z(t)$. To treat the FSI with the submerged structure, we introduce the additive decomposition

$$\phi = \phi^{\text{amb}} + \phi^{\text{per}} \tag{1}$$

of the velocity potential, where the main unknown ϕ^{per} of the exterior flow problem is sought in the whole fluid domain exterior to the structure (i.e. we elect as an engineering approximation to disregard the remote bubble geometry in the definition of ϕ^{per}). The ambient potential ϕ^{amb} decays at infinity, and the same is assumed for ϕ, and hence for ϕ^{per}.

The bubble oscillation may create significant motion of the fluid and the submerged structure. The domain $\Omega_{\text{S}}(t)$ occupied by the structure is thus *a priori* time-dependent, hence so are the fluid domain $\Omega_{\text{F}} := \mathbb{R}^3 \setminus \overline{\Omega_{\text{S}}(t)}$ and the wet surface $\Gamma(t) := \partial\Omega_{\text{F}}(t) \cap \partial\Omega_{\text{S}}(t)$. The structure is assumed to be a linearly elastic solid; other small-strain models involving structural elements such as plates or shells, or history-dependent constitutive models, may be accommodated without major changes.

2.2 Governing equations. The displacement $\mathbf{u}$, stress tensor $\boldsymbol{\sigma}$, perturbed velocity potential ϕ^{per} and fluid pressure p involved in the coupled FSI problem of interest are governed by the structure evolution field equations

$$\begin{cases} \text{(a)} \quad \rho_{\text{S}}\ddot{\mathbf{u}} - \operatorname{div}\boldsymbol{\sigma}(\mathbf{u}) = \mathbf{f}_v, \qquad \text{(b)} \quad \mathbf{u}(\cdot,0) = \dot{\mathbf{u}}(\cdot,0) = \mathbf{0}, \\ \qquad \text{(c)} \quad \text{constitutive relation between } \boldsymbol{\sigma} \text{ and } \mathbf{u} \end{cases} \qquad \text{in } \Omega_{\text{S}}(t)\times[0,T], \tag{2}$$

(which typically correspond to small-strain linearly elastic deformation), the fluid field equations

$$\begin{cases} \text{(a)} \quad \Delta\phi^{\text{per}} = 0, \quad \phi^{\text{per}} \to 0 \text{ at infinity} \\ \text{(b)} \quad p = C - \rho_{\text{F}}\partial_t\phi - \dfrac{\rho_{\text{F}}}{2}|\nabla\phi|^2 - \rho_{\text{F}} g x_3 \end{cases} \qquad \text{in } \mathbb{R}^3 \setminus \overline{\Omega_{\text{S}}(t)}\times[0,T], \tag{3}$$

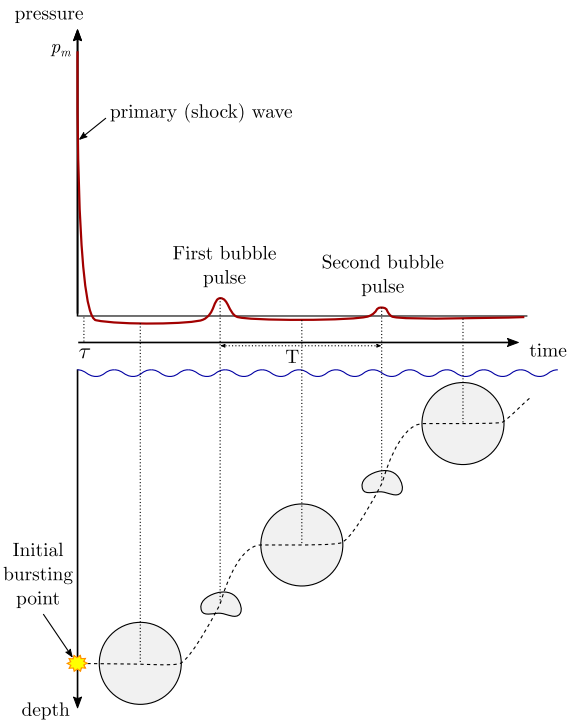

Figure 2: *Schematic representation of the bubble motion and the pressure history, after [31].*

the kinematic continuity condition

$$\partial_{\mathbf{n}}\phi^{\mathrm{per}} = -\partial_n\phi^{\mathrm{amb}} + \dot{\mathbf{u}}\cdot\mathbf{n} \qquad \text{in } \Gamma(t)\times[0,T], \tag{4}$$

and the dynamic continuity condition

$$\boldsymbol{\sigma}(\mathbf{u})\cdot\mathbf{n} = -p\,\mathbf{n} \qquad \text{in } \Gamma(t)\times[0,T], \tag{5}$$

where $\mathbf{n}$ is the normal to the wet surface $\Gamma(t)$ pointing into the fluid, $\rho_{\mathrm{S}}, \rho_{\mathrm{F}}$ are the mass densities of the solid and fluid media, $\mathbf{f}_v$ are external body forces exerted on the solid, g is the gravity. Bernoulli's equation (3b), which features a space-independent function $C(t)$ that will prove to be irrelevant, makes the overall FSI problem defined by equations (2) to (5) nonlinear; in particular, the decomposition (1) cannot be used in (3b), which must be applied to the total potential ϕ. By contrast, the decomposition (1) is used in the linear equations (3a) and (4)

By taking the fluid domain $\Omega_{\mathrm{F}}(t)$ in the FSI system (2)–(5) as $\mathbb{R}^3\setminus\overline{\Omega_{\mathrm{S}}(t)}$, we ignore the region of $\Omega_{\mathrm{F}}(t)$ occupied by the gas bubble. This is a reasonable engineering simplification when considering remote enough explosions: ϕ^{per} spatially decays away from the wet surface, so that taking into account the gas bubble in the definition of ϕ^{per} would alter only moderately the flow solution in the vicinity of the wet surface, which supports the quantities of primary engineering interest.

2.3 Step-by-step iterative coupling. The transient FSI problem defined by equations (2) to (5) is to be solved by means of a time-stepping scheme: we introduce a sequence $t_n = n\Delta t$ $(0\le n\le M)$ of $M+1$ discrete time instants (using for simplicity a constant time step Δt) and aim at finding the time-discrete values $(\mathbf{u}_n, \boldsymbol{\sigma}_n, \phi_n, p_n) = (\mathbf{u}, \boldsymbol{\sigma}, \phi, p)(t_n)$ of the field variables, which are defined on the current solid domain $\Omega_{\mathrm{S}}^n := \Omega_{\mathrm{S}}(t_n)$ and wet surface $\Gamma^n := \Gamma(t_n)$. We treat the coupling problem incrementally in time:

having computed the time-discrete solution up to time $t = t_{n-1}$ included, the solution $(\mathbf{u}_n, \boldsymbol{\sigma}_n, \phi_n, p_n)$ at time $t = t_n$ is to be found by a *sub-cycling* approach, i.e. by alternating solutions in the fluid domain and in the solid domain. Specifically, the k-th sub-cycling iteration consists in

(i) Solving the exterior potential flow problem in $\mathbb{R}^3 \setminus \overline{\Omega_{\mathrm{S}}^n}$ for the unknown $\phi_n^{k,\mathrm{per}}$ defined by equation (3a) and the Neumann boundary condition

$$\partial_n \phi_n^{k,\mathrm{per}} = -\partial_n \phi_n^{\mathrm{amb}} + \dot{\mathbf{u}}_n^{k-1} \cdot \mathbf{n} \qquad \text{on } \Gamma_n, \tag{6}$$

obtained from the kinematic interface condition (4), then setting $\phi_n^k := \phi_n^{k,\mathrm{per}} + \phi_n^{\mathrm{amb}}$ and evaluating the pressure p_n^k on Γ_n by Bernoulli's equation (3b);

(ii) Solving the structure equations (2) in Ω_{S}^n at $t = t_n$ for $(\mathbf{u}, \boldsymbol{\sigma}) = (\mathbf{u}_n, \boldsymbol{\sigma}_n)$ with the Neumann boundary condition

$$\boldsymbol{\sigma}(\mathbf{u}_n^k) \cdot \mathbf{n} = -p_n^k \, \mathbf{n} \qquad \text{on } \Gamma_n \tag{7}$$

The BEM is applied to problem (i), while problem (ii) is solved with one step of a FEM-based time-marching scheme. The solid domain and wet surface are updated via

$$\Omega_{\mathrm{S}}^{n,k+1} = \Omega_{\mathrm{S}}^{n,k} + \mathbf{u}_n^k, \qquad \Gamma_n^{k+1} = \Gamma_n^k + \mathbf{u}_n^k|_{\Gamma_n^k},$$

which in practice means that all nodal coordinates are incremented by the nodal value of u_n^k, the mesh connectivity remaining unchanged. Sub-cycling then continues until a stagnation criterion of the form

$$\|\ddot{\mathbf{u}}_n^k - \ddot{\mathbf{u}}_n^{k-1}\|_{L^2(\Gamma_n)} \le \varepsilon_{\mathrm{sc}} \|\ddot{\mathbf{u}}_n^{k-1}\|_{L^2(\Gamma_n)} \tag{8}$$

is verified by the solid acceleration on Γ_n, where $\varepsilon_{\mathrm{sc}}$ is a preset tolerance.

For the first sub-cycle ($k = 1$), an initialization must be provided for the Neumann datum $\dot{\mathbf{u}}_n^0$ in (6); this is discussed in Sec. 4.2. Choosing $\dot{\mathbf{u}}_n^0$ properly is important, as a good guess can significantly reduce the number of sub-cycles, and hence the overall computational work. Moreover, the kinematic boundary condition (7) can be replaced by a relaxed version to enhance convergence, see (26).

2.4 Boundary element method for the Laplace equation. We use the BEM for solving the potential flow component of the coupled problem, i.e. problem (i) above. The classical direct integral equation relating the unknown Dirichlet trace on $\Gamma(t)$ of the velocity potential ϕ (harmonic in the exterior domain $\Omega_{\mathrm{F}}(t)$ at time $t \in [0, T]$) to the prescribed Neumann datum q such that $\partial_n \phi = -q$ reads [3, 7]

$$\tfrac{1}{2}\phi(\mathbf{y}, t) - \mathcal{H}\{\phi(\cdot, t), t\}(\mathbf{y}) = \mathcal{G}\big\{ q(\cdot, t), t \big\}(\mathbf{y}) \qquad \mathbf{y} \in \Gamma(t)\,, \tag{9}$$

where $\mathcal{G}\{\cdot, t\}$ and $\mathcal{H}\{\cdot, t\}$ are the single- and double-layer integral operators, defined on the surface $\Gamma(t)$ by

$$\mathcal{G}\{q, t\}(\mathbf{y}) = \int_{\Gamma(t)} G(\mathbf{x} - \mathbf{y}) q(\mathbf{x}) \, \mathrm{d}\Gamma(\mathbf{x}), \qquad \mathcal{H}\{\phi, t\}(\mathbf{y}) = \int_{\Gamma(t)} \partial_n G(\mathbf{x} - \mathbf{y}) \phi(\mathbf{x}) \, \mathrm{d}\Gamma(\mathbf{x}).$$

in terms of the (time-independent) *free space fundamental solution* of the Laplace equation, given by

$$G(\mathbf{x} - \mathbf{y}) = \frac{1}{4\pi |\mathbf{x} - \mathbf{y}|}. \tag{10}$$

Upon introducing the discrete time instants t_n and a standard boundary element discretization of $\Gamma_n = \Gamma(t_n)$, $\phi_n := \phi(\cdot, t_n)$ and $\partial_{\mathbf{n}} \phi_n := \partial_{\mathbf{n}} \phi(\cdot, t_n)$, equation (9) yields linear systems of the form

$$[\mathbf{H}_n]\{\boldsymbol{\phi}_n\} = [\mathbf{G}_n]\{\mathbf{Q}_n\}\,, \quad n = 0, 1, \ldots, M, \tag{11}$$

where the N-vectors $\{\boldsymbol{\phi}_n\}$, $\{\mathbf{Q}_n\}$ collect the degrees of freedom (DOFs) for the discrete versions of $\phi(\cdot, t_n)$ and $-\partial_{\mathbf{n}} \phi(\cdot, t_n)$ on the wet surface, while $[\mathbf{G}_n]$, $[\mathbf{H}_n]$ are $N \times N$ matrix discretizations of the integral operators $\mathcal{G}\{\cdot, t_n\}$ and $\frac{1}{2}\mathcal{I} - \mathcal{H}\{\cdot, t_n\}$. In this work, we use standard three-noded flat triangular boundary elements and piecewise-linear, continuous interpolations of ϕ and $\partial_{\mathbf{n}} \phi$. The systems (11) depend on discrete time through (i) the Neumann datum $\{\mathbf{Q}_n\}$ and (ii) the wet surface Γ_n.

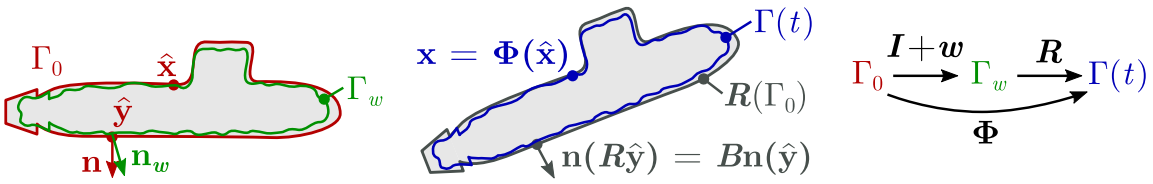

Figure 3: *Decomposition of the displacement into rigid and deformation motions, notations.*

3 Accelerated fluid BEM solver

When dealing, as here, with potential flows, the BE mesh of the wet surface must allow accurate enough modeling of the geometrical details, but is not additionally constrained by wavelength / frequency considerations as in the shock wave case [27]. Our target applications typically require $N \sim 10^4 - 10^5$ velocity potential DOFs on Γ, $M \sim 10^3 - 10^4$ time steps, and multiple BEM solves per time step due to sub-cycling. Solving $O(M)$ BEM problems of size N remains too expensive, however, unless BEM matrices can be reused in compressed form at each time step and sub-cycling iteration. For this reason, accelerating the BEM by means of the fast multipole method (FMM) is ill-suited to the present needs: each new BEM solution would have to be computed more or less from scratch, resulting in a $O(MN)$ overall computational work [28]. By contrast, a preliminary computation and storage of compressed versions of the single- and double-layer integral operators by the $\mathcal{H}$-matrix method is well-suited to solving many BEM problems governed by the same integral operator. While the latter characteristic is not *a priori* true in the present context due to the wet surface being time-dependent (see Section 2.4), integral operator reusability is nevertheless achievable, as explained next in Section 3.1, allowing us to take advantage of $\mathcal{H}$-matrix acceleration for each BEM solution required by the step-by-step FSI iterations (see Sec. 3.2). Moreover, $\mathcal{H}$-matrix compression is known to be efficient for operators whose kernel is asymptotically smooth, a property that the Laplace kernel (10) enjoys [5].

3.1 Reusing integral operators.

Let Γ_n and Γ_0 respectively denote the current and initial configurations of the wet surface, and let $\boldsymbol{\Phi}_n$ be the deformation taking Γ_0 to Γ_n: using a Lagrangian description and omitting the discrete time index n for brevity, the current position $\mathbf{x}$ on Γ of a material point is related to its initial position $\hat{\mathbf{x}}$ on Γ_0 through

$$\mathbf{x} = \boldsymbol{\Phi}(\hat{\mathbf{x}}) \qquad (\hat{\mathbf{x}} \in \Gamma_0, \mathbf{x} \in \Gamma)$$

In practice, the action of $\boldsymbol{\Phi}$ is computed by sequentially updating the wet surface using the converged kinematic response of the structure at each time step (see Sec. 2.3).

To cater for a potentially significant rigid-body contribution to the wet surface deformation, $\boldsymbol{\Phi}$ is assumed to have the form

$$\boldsymbol{\Phi} = \mathbf{R} \circ (\mathbf{I} + \mathbf{w}), \quad \text{i.e.} \quad \mathbf{x} = \mathbf{R}(\hat{\mathbf{x}} + \mathbf{w}(\hat{\mathbf{x}})) \qquad (\hat{\mathbf{x}} \in \Gamma_0, \mathbf{x} \in \Gamma) \tag{12}$$

where $\mathbf{w}$ is a displacement field and $\mathbf{R}$ describes a rigid-body motion (RBM), see Fig. 3. The decomposition (12) can be formulated with $\mathbf{R}$ chosen arbitrarily: given $\boldsymbol{\Phi}$, choose a RBM $\mathbf{R}$ and set $\mathbf{w} := \mathbf{R}^{-1}\boldsymbol{\Phi} - \mathbf{I}$. A sensible choice for $\mathbf{R}$ may be found by solving the minimization problem

$$\min_{\boldsymbol{c},\mathbf{B}} \|\boldsymbol{\Phi} - \mathbf{R}\|^2_{L^2(\Gamma_0)}, \qquad \mathbf{R}\hat{\mathbf{x}} = \mathbf{R}[\boldsymbol{c}, \mathbf{B}](\hat{\mathbf{x}}) = \boldsymbol{c} + \mathbf{B}\hat{\mathbf{x}} \tag{13}$$

which, since $|\boldsymbol{\Phi}(\hat{\mathbf{x}}) - \mathbf{R}\hat{\mathbf{x}}| = |\mathbf{w}(\hat{\mathbf{x}})|$, aims at finding the smallest (in the $L^2(\Gamma_0)$ norm sense) non-rigid displacement $\mathbf{w}$. In (13), the generic RBM $\mathbf{R}$ is expressed in terms of a translation vector $\boldsymbol{c} \in \mathbb{R}^3$ and

a rotation matrix $\mathbf{B} \in \mathbb{R}^{3\times 3}$ satisfying $\mathbf{B}^{\mathrm{T}}\mathbf{B} = \mathbf{B}\mathbf{B}^{\mathrm{T}} = \mathbf{I}$ and $\mathrm{Det}(\mathbf{B}) = 1$, and is thus determined (for three-dimensional configurations) by 6 scalar parameters.

The current velocity potential ϕ is governed by the BIE (9) written on the current wet surface Γ. To determine the effect of the wet surface change on the BIE, we reformulate it on the fixed (initial) surface Γ_0 by setting $\mathbf{x} = \mathbf{R}(\hat{\mathbf{x}}+\mathbf{w}(\hat{\mathbf{x}}))$ and introducing the convected versions on Γ_0 of the datum and unknown potential, respectively given by $\hat{q} := q\circ\mathbf{\Phi}$ and $\hat{\phi} := \phi\circ\mathbf{\Phi}$. This reformulation relies on the key observations that we have

$$\mathbf{n}(\mathbf{R}\mathbf{x}) = \mathbf{B}\mathbf{n}(\mathbf{x}), \qquad \mathrm{d}\Gamma(\mathbf{R}\mathbf{x}) = \mathrm{d}\Gamma(\mathbf{x})$$

and, by virtue of the isotropy and translational invariance of the kernel G,

$$G(\mathbf{R}\mathbf{x}-\mathbf{R}\mathbf{y}) = G(\mathbf{x}-\mathbf{y}), \qquad \mathbf{n}(\mathbf{R}\mathbf{x})\cdot\boldsymbol{\nabla}G(\mathbf{R}\mathbf{x}-\mathbf{R}\mathbf{y}) = \mathbf{n}(\mathbf{x})\cdot\boldsymbol{\nabla}G(\mathbf{x}-\mathbf{y}) = \partial_{\mathbf{n}(\mathbf{y})}G(\mathbf{x}-\mathbf{y})$$

for any RBM $\mathbf{R}$. As a result, the BIE (9) is recast as

$$\frac{1}{2}\hat{\phi}(\hat{\mathbf{y}}) - \int_{\Gamma_0} \mathbf{n}_w(\hat{\mathbf{x}})\cdot\boldsymbol{\nabla}G\big(\hat{\mathbf{x}}-\hat{\mathbf{y}}+\mathbf{w}(\hat{\mathbf{x}})-\mathbf{w}(\hat{\mathbf{y}})\big)\,\hat{\phi}(\hat{\mathbf{x}})J(\hat{\mathbf{x}})\,\mathrm{d}\Gamma(\hat{\mathbf{x}}) = \int_{\Gamma_0} G\big(\hat{\mathbf{x}}-\hat{\mathbf{y}}+\mathbf{w}(\hat{\mathbf{x}})-\mathbf{w}(\hat{\mathbf{y}})\big)\,\hat{q}(\hat{\mathbf{x}})J(\hat{\mathbf{x}})\,\mathrm{d}\Gamma(\hat{\mathbf{x}}), \qquad \hat{\mathbf{y}}\in\Gamma_0 \quad (14)$$

wherein $J := \|(\mathbf{I}+\boldsymbol{\nabla}\mathbf{w})^{-\mathrm{T}}\mathbf{n}\|\,\mathrm{Det}(\mathbf{I}+\boldsymbol{\nabla}\mathbf{w})$ is the surface Jacobian of the mapping $\mathbf{I}+\mathbf{w}$ (see e.g. [19], Def. 5.4.2) and $\mathbf{n}_w := (\mathbf{I}+\boldsymbol{\nabla}\mathbf{w})^{-\mathrm{T}}\mathbf{n}\,/\,\|(\mathbf{I}+\boldsymbol{\nabla}\mathbf{w})^{-\mathrm{T}}\mathbf{n}\|$ is the unit normal on $\Gamma_w := (\mathbf{I}+\mathbf{w})\Gamma_0$ (see e.g. [19], Prop. 5.4.14). Equation (14) is readily seen to be the BIE formulation of the potential flow problem in the domain Ω_w exterior to the deformed surface Γ_w defined by

$$\Delta\hat{\phi}_w = 0 \ \text{ in } \Omega_w, \qquad \partial_{\mathbf{n}}\hat{\phi}_w = \hat{q}_w \ \text{ on } \Gamma_w, \qquad |\hat{\phi}_w(\mathbf{x})| = O(|\mathbf{x}|^{-2}) \ \text{ at infinity} \quad (15)$$

where $\hat{\phi}_w := \hat{\phi}\circ(\mathbf{I}+\mathbf{w})^{-1} = \phi\circ\mathbf{R}$ and $\hat{q}_w := \hat{q}\circ(\mathbf{I}+\mathbf{w})^{-1} = g\circ\mathbf{R}$ are the convected versions on Γ_w of $\hat{\phi}$ and $\hat{q}$. In other words, solving the BIE (9) is equivalent to solving the BIE (14) or the exterior boundary-value problem (15), with $\mathbf{R}$ and $\mathbf{w}$ related to $\mathbf{\Phi}$ through (12).

For any purely rigid deformation $\mathbf{\Phi}$ (i.e. $\mathbf{\Phi} = \mathbf{R}$ for some RBM $\mathbf{R}$), the convected BIE (14) and the associated exterior problem (15) holds with $\mathbf{w} = \mathbf{0}$; we have $\hat{\phi}_w = \hat{\phi}_0 = \hat{\phi}$, $\hat{q}_w = \hat{q}_0 = \hat{q}$, and the BIE (9) becomes

$$\frac{1}{2}\hat{\phi}_0(\hat{\mathbf{y}}) - \int_{\Gamma_0} \mathbf{n}(\hat{\mathbf{x}})\cdot\boldsymbol{\nabla}G(\hat{\mathbf{x}}-\hat{\mathbf{y}})\,\hat{\phi}_0(\hat{\mathbf{z}})\,\mathrm{d}\Gamma(\hat{\mathbf{x}}) = \int_{\Gamma_0} G(\hat{\mathbf{x}}-\hat{\mathbf{y}})\,\hat{q}(\hat{\mathbf{x}})\,\mathrm{d}\Gamma(\hat{\mathbf{x}}). \quad (16)$$

Consequently, if the FSI induces a purely rigid motion of $\Gamma(t)$, all potential flow problems arising can be set as Laplace BIEs on the initial surface Γ_0; the integral operators are constant, and hence reusable. If $\Gamma(t)$ evolves in a "mostly rigid" manner in time (i.e. if the non-rigid displacement $\mathbf{w}(\cdot,t)$ is small enough, in a sense made more precise below by (18), at all times), we can still solve problem (9) approximately by setting $\mathbf{w} = \mathbf{0}$ (i.e. neglecting the effect of $\mathbf{w}$) in (14) and solving (16) for $\hat{\phi}_0$.

Practical operator reuse. The practical outcome of the foregoing analysis is quite simple. The initial BEM-discretized operators $\mathbf{H}_0$, $\mathbf{G}_0$ are computed once (as data-sparse approximations, see Sec. 3.2). The current surface $\Gamma = \mathbf{\Phi}(\Gamma_0)$ is monitored by sequentially updating the nodal positions of the boundary elements using the structure incremental kinematic response, the BE mesh connectivity being conserved. The correspondence between ϕ and $\hat{\phi}_0$ reduces to $\{\boldsymbol{\phi}\} = \{\hat{\boldsymbol{\phi}}_0\}$ (with $\{\boldsymbol{\phi}\}$ and $\{\hat{\boldsymbol{\phi}}_0\}$ understood as values attached to nodes of the BEM meshes of Γ and Γ_0 that correspond to each other

by convection) and likewise $\{\mathbf{Q}\} = \{\hat{\mathbf{Q}}_0\}$ with the same interpretation. Therefore, if the wet surface moves in a mostly rigid manner, the BE systems (11) are simply approximated as

$$[\mathbf{H}_0]\{\boldsymbol{\phi}_n\} = [\mathbf{G}_0]\{\mathbf{Q}_n\}\,, \quad n = 0, 1, \ldots, M, \tag{17}$$

where in particular the discrete Neumann datum vector $\{\mathbf{Q}_n\}$ holds the values of the Neumann datum q_n computed at the nodal locations of the current surface Γ_n and using its unit normal.

Solution error caused by operator reuse. The difference $\hat{\phi}_w - \hat{\phi}_0$, i.e. the approximation error $\phi - \phi_0$ incurred by reusing the integral operators defined on Γ_0, may be estimated with the help of the theory of shape differentiation of boundary-value problems [19]. Subject to sufficient regularity of Γ_0 and g, solutions $\hat{\phi}_w$ of interior boundary value problems similar to (15) are differentiable w.r.t. $\mathbf{w}$ in a neighborhood of $\mathbf{w} = \mathbf{0}$ (at which the approximation $\hat{\phi}_0$ is evaluated), the relevant norm for $\mathbf{w}$ being the $W^{1,\infty}$ norm defined (on extensions to $\mathbb{R}^3$ of $\mathbf{w}$) by

$$\|\mathbf{w}\|_{1,\infty} := \sup_{\mathbf{x},\mathbf{y}\in\mathbb{R}^3,\, \mathbf{y}\neq\mathbf{x}} \Big(|\mathbf{w}(\mathbf{y})| + \frac{|\mathbf{w}(\mathbf{y}) - \mathbf{w}(\mathbf{x})|}{|\mathbf{y} - \mathbf{x}|} \Big). \tag{18}$$

This implies an approximation error $\hat{\phi}_w - \hat{\phi}_0$ that is linear in $\mathbf{w}$ for small enough $\|\mathbf{w}\|_{1,\infty}$. This is an acceptable approximation for small distortions of the shape of $\Gamma(t)$, an assumption for example implicitly made when the chosen structure model assumes small strains. Moreover, the shape differentiation framework gives the option of refining the foregoing small-$\mathbf{w}$ approximation: first-order (in $\mathbf{w}$) corrections of $\hat{\phi}_w$ can be found by solving additional BIEs that result from differentiating (14) w.r.t. $\mathbf{w}$ at $\mathbf{w} = \mathbf{0}$, the unknowns of the latter being also governed by the same fixed integral operators.

3.2 $\mathcal{H}$-matrix acceleration.

We just determined conditions under which the flow problems arising in the sub-cycling iterations can acceptably be formulated using the fixed BEM matrices $\mathbf{H}_0$ and $\mathbf{G}_0$. This makes it attractive to precompute data-sparse approximations of $\mathbf{H}_0$ and $\mathbf{G}_0$ based on hierarchical matrices, or $\mathcal{H}$-matrices. This task rests on existing methods pertaining to $\mathcal{H}$-matrices, which we concisely describe thereafter for completeness. Our $\mathcal{H}$-matrix solver for the BEM systems (17) is implemented in the in-house fast BEM code [9]. Since a large number of problems (17) have to be solved, the data-sparse $\mathcal{H}$-BEM matrices are stored in RAM memory to reduce the time spent reading them this many times.

$\mathcal{H}$-matrix representation. Originally introduced by Hackbush [18], $\mathcal{H}$-matrices aim at computing data-sparse approximations of dense matrices $\mathbb{A} \in \mathbb{R}^{N\times N}$ such as $\mathbf{H}_0$ and $\mathbf{G}_0$. The general idea is to (i) partition $\mathbb{A}$ into blocks and (ii) find low-rank approximations of those blocks known *a priori* to be amenable to this treatment. Here, the same set of indices $I = \{1, \ldots, N\}$ can be used for numbering the rows and columns of BEM matrices $\mathbb{A}$. Blocks are sub-matrices $\mathbb{A}_{\sigma\times\tau}$ of $\mathbb{A}$, where $\sigma \subset I$ and $\tau \subset I$ are subsets of row and column indices of $\mathbb{A}$, corresponding to clusters X_σ, X_τ of collocation and interpolation nodes of the BE mesh. For the present Laplace case, blocks that are deemed admissible (i.e. admit accurate low-rank approximations) satisfy the *η-admissibility criterion*

$$\min\big(\mathrm{diam}(X_\sigma),\, \mathrm{diam}(Y_\tau)\big) \leq \eta\, \mathrm{dist}\big(\mathrm{diam}X_\sigma, Y_\tau\big),$$

where $\mathrm{diam}(X)$ and $\mathrm{dist}(X, Y)$ are the diameter of a cluster X and the Euclidean distance between clusters X, Y, respectively. In particular, diagonal blocks (such that $\sigma = \tau$) are not deemed admissible: they contain the contributions of singular integrals and have full numerical rank as a result.

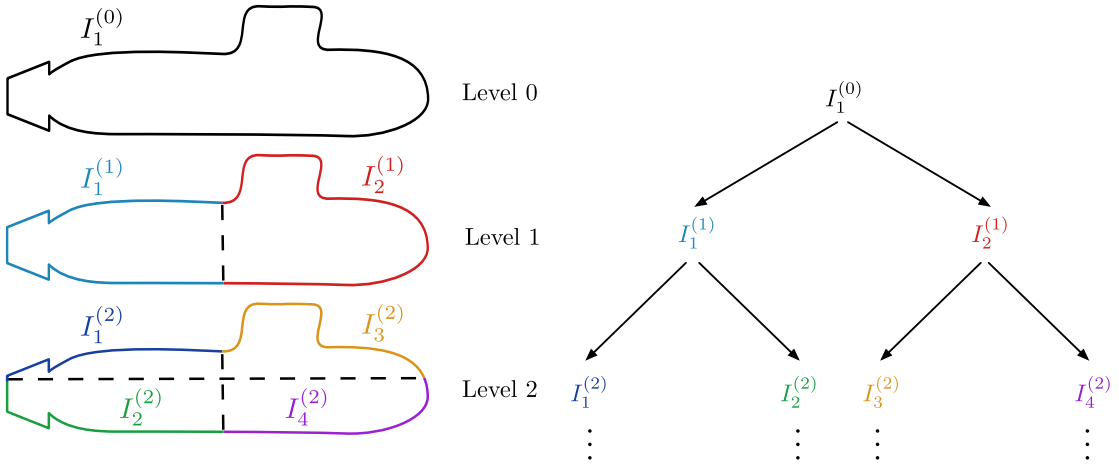

(a) Partition of the physical domain (b) Binary cluster tree $\mathcal{T}_I$

Figure 4: *Illustration of the clustering of the degrees of freedom: (a) partition of the DOFs of a submarine, and (b) corresponding binary tree. After [8].*

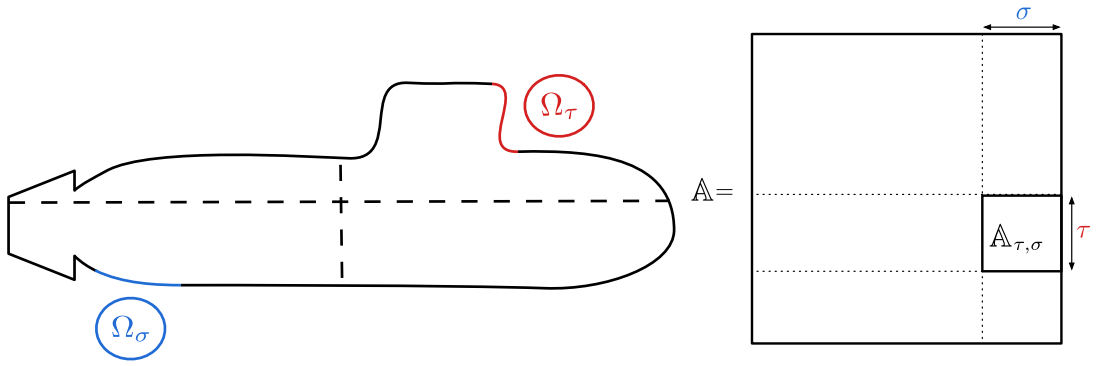

(a) (b)

Figure 5: *Illustration of the construction of the block cluster tree: (a) clustering of the unknowns on the geometry and (b) corresponding block clustering in the matrix. After [8].*

Hierarchical clustering of the unknowns. To maximize the proportion of entries of $\mathbb{A}$ belonging to η-admissible blocks while keeping some of the latter large, which are conflicting goals, the block subdivision is recursive. This key ingredient is implemented by defining a binary tree $\mathcal{T}_I$. Each node of $\mathcal{T}_I$ defines a subset $\sigma \subset I$ of indices, i.e. a cluster X_σ of nodes. Sets σ are recursively partitioned into two subsets, i.e. $\sigma = \sigma_1 \cup \sigma_2$, until their size $|\sigma|$ satisfies $|\sigma| \leq n_{\text{leaf}}$ (where n_{leaf} is given). The subdivision starts from the root node containing the complete set of indices $\sigma = I$ (see Fig. 4). Once determined, the binary tree $\mathcal{T}_I$ is used to define a block cluster representation $\mathcal{T}_{I\times I}$ of $\mathbb{A}$, each node of $\mathcal{T}_{I\times I}$ containing an ordered pair (σ, τ) of index sets of $\mathcal{T}_I$ associated to block $\mathbb{A}_{\sigma\times\tau}$ (see Fig. 5). Finally, a non-uniform partition $\mathcal{P}$ of $\mathbb{A}$ into blocks is defined by tracing the branches of $\mathcal{T}_{I\times I}$ from the root node, recursively subdividing any encountered block $\mathbb{A}_{\sigma\times\tau}$ into 2×2 sub-blocks until $\mathbb{A}_{\sigma\times\tau}$ is either η-admissible or too small (i.e. $\min(|\sigma|, |\tau|) \leq n_{\text{leaf}}$); $\mathcal{P}$ then collects all nodes at which subdivision is stopped. This treatment in particular produces admissible blocks that are as large as possible. The partition $\mathcal{P}$ is divided into two sub-partitions $\mathcal{P}_{\text{ad}}$ and $\mathcal{P}_{\text{non-ad}}$, holding respectively all admissible and non-admissible blocks.

Low-rank block approximation. Various methods allow to compute low-rank approximations of admissible blocks. The truncated singular value decomposition [16] produces approximations of smallest

rank for prescribed accuracy ε in spectral or Frobenius norm, but at a computational and memory cost that is excessive for large-scale problems. The adaptive cross approximation (ACA) [6] yields quasi-optimal low-rank approximations without requiring that complete blocks be computed and assembled. The ACA iteratively improves an approximation $\mathbb{B}_k$ of a block $\mathbb{B} \in \mathbb{R}^{m\times n}$ by adding rank-1 matrices: $\mathbb{B}_k = \sum_{\ell=1}^{k} \mathbf{u}_\ell \mathbf{v}_\ell^{\mathrm{T}}$ with $\mathbf{u}_\ell \in \mathbb{R}^m$, $\mathbf{v}_\ell \in \mathbb{R}^n$. The truncation error can be monitored, and ACA stops at rank $k=r$ such that $\|\mathbb{B}-\mathbb{B}_r\|_{\mathrm{F}} \leq \varepsilon_{\mathrm{ACA}}\|B\|_{\mathrm{F}}$, where $\|\cdot\|_{\mathrm{F}}$ denotes the Frobenius norm, and $\varepsilon_{\mathrm{ACA}} > 0$ is a preset tolerance. The rank-r approximation $\mathbb{B}_r$ is completely defined by the r pairs of vectors $(\mathbf{u}_\ell, \mathbf{v}_\ell)$, which are stored at a $O\big(r(m+n)\big)$ memory cost. Contributions of block $\mathbb{B}$ to matrix-vector products $\mathbb{A}\boldsymbol{\phi}$ are evaluated as $\mathbb{B}\boldsymbol{\phi} \approx \sum_{\ell=1}^{r} \big(\mathbf{v}_\ell^{\mathrm{T}}\boldsymbol{\phi}\big)\mathbf{u}_\ell$. We use the ACA algorithm described in [8], whose computational complexity for approximating a given block $\mathbb{B} \in \mathbb{R}^{m\times n}$ to rank r is $O\left(r^2(m+n)\right)$.

Resulting $\mathcal{H}$-BEM. To solve problems (17) efficiently, data-sparse approximations $\mathbf{H}_{0,\varepsilon,\eta}$, $\mathbf{G}_{0,\varepsilon,\eta}$ of $\mathbf{H}_0$, $\mathbf{G}_0$ such that $\|\mathbf{H}_{0,\varepsilon,\eta}-\mathbf{H}_0\| \leq \varepsilon\|\mathbf{H}_0\|$ and $\|\mathbf{G}_{0,\varepsilon,\eta}-\mathbf{G}_0\| \leq \varepsilon\|\mathbf{G}_0\|$ are computed using the foregoing methodology. Problems (17) are then replaced with their $\mathcal{H}$-matrix approximations

$$[\mathbf{H}_{0,\varepsilon,\eta}]\{\boldsymbol{\phi}_n^k\} = [\mathbf{G}_{0,\varepsilon,\eta}]\{\mathbf{Q}_n^k\}, \tag{19}$$

which for each right-hand side $\{\mathbf{Q}_n^k\}$ is solved iteratively by means of the GMRES algorithm [29]. The overall FSI process entails many matrix-vector products, whose memory requirement and cost is much reduced thanks to the data-sparse character of $\mathbf{H}_{0,\varepsilon,\eta}$ and $\mathbf{G}_{0,\varepsilon,\eta}$.

3.3 Pressure evaluation on the wet surface.

The evaluation of the fluid pressure on Γ by means of Bernoulli's equation (3b), being involved in the dynamic boundary condition (7), is a key part of the sub-cycling process. It entails computing $\partial_t\phi$ and $|\boldsymbol{\nabla}\phi|^2$ by post-processing the BEM solution for ϕ:

- The time derivative $\partial_t\phi$ is evaluated pointwise on Γ using the backward differentiation formula of order 4 (BDF4), except for the first time steps where lower-order BDF1, BDF2 or BDF3 formulas are used depending on the number of available past values of ϕ.
- The velocity potential gradient is decomposed as $\boldsymbol{\nabla}\phi = \boldsymbol{\nabla}_\Gamma\phi + (\partial_{\mathbf{n}}\phi)\mathbf{n}$, where the normal derivative $\partial_{\mathbf{n}}\phi$ is known from the kinematic boundary condition (6) while the surface gradient $\boldsymbol{\nabla}_\Gamma\phi$ is evaluated on each element by differentiating the BEM interpolation of the nodal values [30]. We then have $|\boldsymbol{\nabla}\phi|^2 = |\boldsymbol{\nabla}_\Gamma\phi| + (\partial_{\mathbf{n}}\phi)^2$.

3.4 Summary of the computational FSI procedure.

We finally summarize the step-by-step $\mathcal{H}$-BEM/FEM coupling procedure.

Pre-computations. The $\mathcal{H}$-BEM operators are computed and stored, then the coupling procedure starts.

Sub-cycling steps. At each time t_n and sub-cycling iteration k, the following steps are carried out:

- Estimate the structure normal velocity $\mathbf{n}\cdot\mathbf{v}_n^k$ (with initial conditions for the case $n=0$) and $\partial_{\mathbf{n}}\phi^{\mathrm{amb}}$ on the updated surface Γ_n^k; compute the Neumann datum for (6).
- Solve (19) for ϕ^{per} (within tolerances $\varepsilon_{\mathrm{GMRES}}$ for GMRES and ε for $\mathcal{H}$-matrix compression).
- Compute p elementwise using Bernoulli's equation (3b) (Sec. 3.3), with $C(t) = 0$ since the pressure has to vanish at infinity, and then the nodal forces $\mathbf{f}$ [34].
- Compute the structure response increment by performing one step of a FEM-based time-marching.
- Check the stagnation convergence criterion: advance to the next time step if (8) is verified, and to the next sub-cycling iteration otherwise.

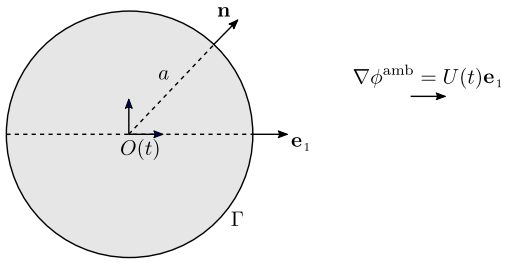

Figure 6: *Rigid sphere in an infinite fluid domain, with uniform ambient flow velocity $U(t)\mathbf{e}_1$. The sphere is either motionless (Sec. 4.1) or mobile with $O(t) = O(0) + d(t)\mathbf{e}_1$ (Sec. 4.2)*

It is possible to guard against the non-rigid deformation of Γ becoming too large over time by checking periodically whether it remains below a preset threshold. This threshold can be defined in terms of the residual of the minimization (13), or alternatively of the mean on Γ_0 of $|\mathrm{div}_S \hat{\mathbf{w}}|$. Should this test fail at some time step, we would update Γ, compute new $\mathcal{H}$-matrix approximations of $\mathbf{G}, \mathbf{H}$ defined on the updated surface, and restart sub-cycling iterations. We have not yet implemented this provision.

4 Validation example: rigid sphere in a uniform flow

We consider a rigid sphere Γ of radius a immersed in an infinite fluid domain, with spatially uniform ambient flow velocity $U(t)\mathbf{e}_1$ for a given time-dependent velocity amplitude $U(t)$, $t \in [0, T]$ (Figure 6). We disregard gravity and its possible effects (buoyant force, hydrostatic pressure) for this example. The ambient velocity potential is thus given at any point $\mathbf{x} = (x_1, x_2, x_3)$ by

$$\phi^{\mathrm{amb}}(\mathbf{x}, t) = U(t) x_1 \,, \tag{20}$$

This configuration allows to validate first the $\mathcal{H}$-matrix BEM solver (motionless sphere case, Sec. 4.1), then the step-by-step coupling procedure (mobile sphere case, Sec. 4.2).

4.1 Motionless sphere. We first consider the case where the sphere is motionless, and centered at the coordinate origin, so that the fluid domain is $\Omega_{\mathrm{F}} := \{\mathbf{x} \in \mathbb{R}^3,\ |\mathbf{x}| > a\}$, see Figure 6. All fluid variables for this problem are known in closed form, see Appendix A; in particular, the net force $f(t)$ exerted by the force density $p(\mathbf{x}, t)\mathbf{n}(\mathbf{x})$ on the motionless sphere is given by

$$\mathbf{f}(t) = -\int_\Gamma p(\mathbf{x}, t)\mathbf{n}(\mathbf{x})\, \mathrm{d}\Gamma(\mathbf{x}) = \tfrac{3}{2} m_{\mathrm{F}} \dot{U}(t)\mathbf{e}_1, \tag{21}$$

where $m_{\mathrm{F}} := 4\pi a^3 \rho_{\mathrm{F}}/3$ is the mass of water that would fill the sphere.

Numerical results were obtained with the following parameters: $\rho_{\mathrm{F}} = 1000$ kg/m^3, $a = 3$ m, $U(t) = U_0 \cos(2\pi f t)$ (with $U_0 = 15.0$ m/s and $f = 4$ Hz), total duration $T = 0.5$ s (two periods) divided into $M = 200$ time steps. The BEM model uses planar triangular elements with piecewise-linear C^0 interpolation, for a total of $N = 2562$ DOFs. The $\mathcal{H}$-matrix approximations of $\mathbf{H}_0$ and $\mathbf{G}_0$ were computed using a minimum block size $n_{\mathrm{leaf}} = 50$ and a relative accuracy threshold equal to 10^{-4}. The GMRES tolerance was set to 10^{-4}.

The computed fluid quantities are in good agreement with their reference analytic values, as shown by the relative errors $E(g; \theta_i)$ on time histories $t \mapsto (g(\theta_i, t))$ at three angular positions θ_i on the sphere ($g = \phi, \partial_t\phi, |\nabla\phi|, p$, $(\theta_1, \theta_2, \theta_3) = (0, 3\pi/10, \pi/2)$) given in Table 1; we have set

$$E^2(g; \theta_1, \theta_2, \theta_3) := \frac{\sum_{i=1}^3 \|g(\theta_i, \cdot) - g^{\mathrm{ref}}(\theta_i, \cdot)\|_T^2}{\sum_{i=1}^3 \|g(\theta_i, \cdot)^{\mathrm{ref}}\|_T^2}, \quad \text{with} \quad \|h\|_T^2 := \int_0^T h^2(t)\, \mathrm{d}t \tag{22}$$

$E(\phi;\theta_i)$	$E(\partial_t\phi;\theta_i)$	$E(\lvert\nabla\phi\rvert^2;\theta_i)$	$E(p;\theta_i)$
$7.4\,10^{-4}$	$3.2\,10^{-3}$	$5.5\,10^{-3}$	$3.2\,10^{-3}$

Table 1: *Motionless sphere: relative errors (see (22)) on fluid quantities against reference analytic values*

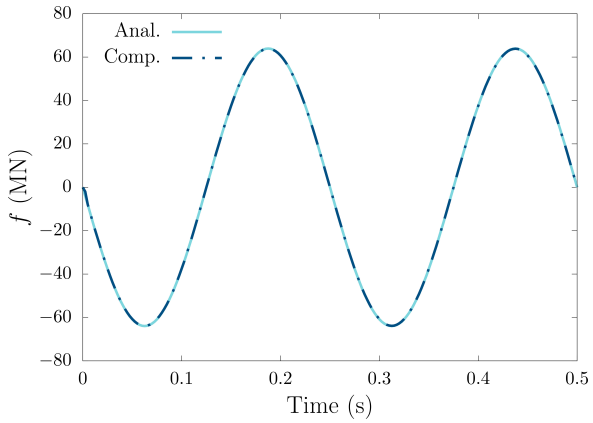

Figure 7: *Motionless sphere: comparison between analytical and computed net force histories.*

and g^{ref} indicating the reference value. The computed axial net force $f(t) := \mathbf{f}(t)\cdot\mathbf{e}_1$ agrees similarly well with its analytical counterpart, as shown in Fig. 7; the relative error $E(f) := \|f - f^{\mathrm{ref}}\|_T/\|f\|_T$ on $t \mapsto f(t)$ is $3.5\,10^{-3}$. This simple example of a motionless sphere validates the $\mathcal{H}$-matrix-based potential flow BEM solver, with the approximations induced by the $\mathcal{H}$-matrix compression, the iterative solver and the BEM discretization still allowing relative errors well below the typical industry target precision of 1% on all fluid variables.

4.2 Mobile rigid sphere. We now study the case where the ambient flow (20) induces a motion of the rigid sphere (see Fig. 6), which provides a validation test for our coupling procedure. The ambient flow still being uniaxial and uniform, the sphere moves along $\mathbf{e}_1$ and its translational displacement $\mathbf{d}(t)$ has the form $\mathbf{d}(t) = d(t)\mathbf{e}_1$. For this example, closed-form solutions are available for all fluid quantities (see Appendix A) as well as the resulting motion $t \mapsto d(t)$ of the sphere, found to be given in terms of the initial conditions $d(0), \dot{d}(0)$ and other parameters of the problem by

$$d(t) = \frac{3m_{\mathrm{F}}}{2m+m_{\mathrm{F}}}\int_0^t \big(U(\tau)-U(0)\big)\,\mathrm{d}\tau + \dot{d}(0)t + d(0)\,, \tag{23}$$

The numerical results are obtained with the same parameters as for the motionless sphere (Sec. 4.1) except for the ambient velocity, here set to $U(t) = A\,t^4(T-t)^4$, with $T = 0.5$ s and $A = 15(0.25)^{-8}$ SI (set such that $U_{\max} = 15$ m/s); moreover, $\dot{d}(0) = 0$ and $m = 2m_{\mathrm{F}}$. At a discrete time t_n, the acceleration $\mathbf{a}_n$ is computed from the nodal forces $\mathbf{f}_n$. Then, assuming a linear variation in time of the acceleration in $[t_{n-1}, t_n]$ and setting $\mathbf{a}_{-1} = \mathbf{v}_{-1} = \mathbf{d}_{-1} = \mathbf{0}$, the velocity and displacement are obtained as

$$\mathbf{v}_n = \tfrac{1}{2}\big(\mathbf{a}_n + \mathbf{a}_{n-1}\big)\Delta t + \mathbf{v}_{n-1}\,, \qquad \mathbf{d}_n = \tfrac{1}{6}\big(\mathbf{a}_n + 2\mathbf{a}_{n-1}\big)\Delta t^2 + \mathbf{v}_{n-1}\Delta t + \mathbf{d}_{n-1}\,.$$

The computed fluid quantities are, again, in good agreement with their reference analytic values, as shown by the relative errors $E(g) := \|g - g^{\mathrm{ref}}\|_T/\|g\|_T$ given (with $\|\cdot\|_T$ again as in (22)) in Table 2 on the time histories of $g = \phi, \partial_t\phi, |\nabla\phi|\mathbf{v}\cdot\nabla\phi, p$ at the same three angular positions on the sphere as in the previous example. The computed response of the submerged mobile sphere is also recovered

	$E(\phi)$	$E(\partial_t\phi)$	$E(\lvert\nabla\phi\rvert^2)$	$E(\mathbf{v}\cdot\nabla\phi)$	$E(p)$	$E(f)$	$E(d)$
$M=200$	$1.7\,10^{-3}$	$2.8\,10^{-3}$	$4.5\,10^{-3}$	$3.7\,10^{-3}$	$3.0\,10^{-3}$	$2.6\,10^{-3}$	$2.2\,10^{-3}$
$M=1000$	$1.5\,10^{-3}$	$2.1\,10^{-3}$	$3.9\,10^{-3}$	$3.3\,10^{-3}$	$2.3\,10^{-3}$	$1.4\,10^{-3}$	$1.5\,10^{-3}$

Table 2: *Mobile sphere: relative errors on histories of fluid quantities, net force f and net displacement d against reference analytical values*

accurately, see the relative errors on the net force and displacement histories given in Table 2. For additional graphical comparison, the computed and reference net force and displacement histories are shown (using $M=200$) in Fig. 8.

The relative error for the acceleration is dictated by $\varepsilon_{\text{sc}}=10^{-3}$. When using $M=200$ time steps, the stagnation tolerance $\varepsilon_{\text{sc}}=10^{-3}$ imposed on the accelerations was found not to be always verified by the velocities, especially at time instants for which the velocity is low. This in turn induces higher relative errors on the other time-dependent quantities at such instants (compensated by the small magnitude of those quantities at such times). When using $M=1000$ time steps, the preset stagnation tolerance ε_{sc} was found to be satisfied by all time-dependent quantities. Note that the choice of ε_{sc} must be consistent with that of the other tolerance values (notably $\varepsilon_{\text{GMRES}}=10^{-4}$ and $\varepsilon=10^{-4}$).

Table 3 shows the average number $\langle N_{\text{sc}}\rangle$ of sub-cycles needed at each time step for the acceleration and velocity to satisfy the stagnation tolerance ε_{sc} (i.e the cumulative number of sub-cycles used for each time step divided by M). For given ε_{sc}, $\langle N_{\text{sc}}\rangle$ mainly depends on M and the quality of the initial guess used for the velocity. Since sub-cycling iterations aim at iteratively finding the normal component of $\mathbf{v}_{n+1}$, the choice of $\mathbf{v}^0_{n+1}$ is of great importance. Setting $\mathbf{v}^0_{n+1}=\mathbf{v}_n$, while quite simple, resulted in too many sub-cycles for $M=200$. We instead considered either the linear guess

$$\mathbf{v}^0_{n+1}=\mathbf{v}_n+\Delta t\,\mathbf{a}_n\,,$$

yielded by a first-order Taylor expansion, or the quadratic guess

$$\mathbf{v}^0_{n+1}=\mathbf{v}_n+\Delta t\,\mathbf{a}_n+\tfrac{1}{2}\Delta t^2\dot{\mathbf{a}}_n\,,$$

where the numerical time derivative of the acceleration is evaluated using the BDF4 scheme. Table 3 shows the obtained values of $\langle N_{\text{sc}}\rangle$ when using either guess. When $M=200$ and $\varepsilon_{\text{sc}}=10^{-2}$, using the quadratic guess results in $\langle N_{\text{sc}}\rangle$ very close to its lowest possible value of 2 (as two sub-cycles are needed in order to check the stagnation-based stopping criterion). The results of Table 3 otherwise

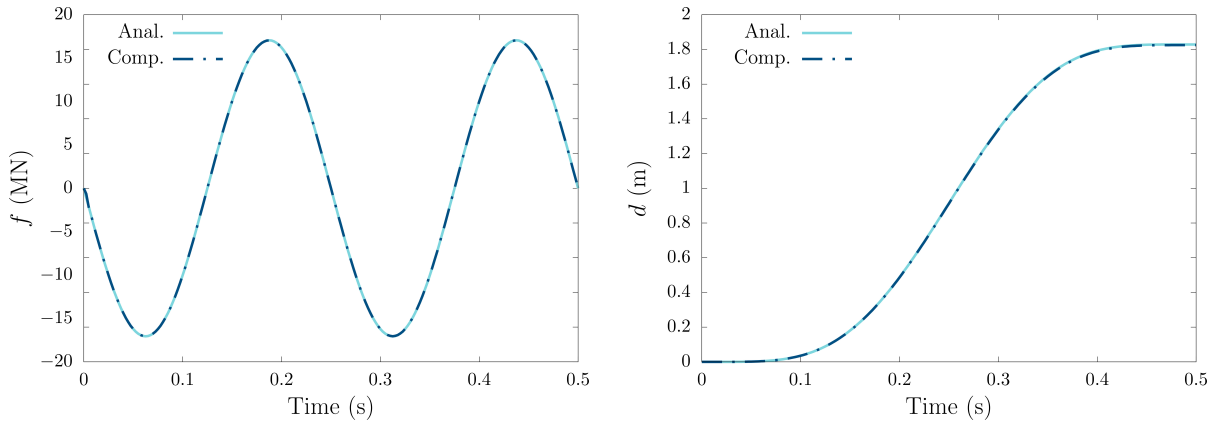

Figure 8: *Mobile sphere: comparison of computed net force and displacement histories (obtained using a quadratic guess for the velocity, $\varepsilon_{sc}=10^{-3}$ and $M=200$) with corresponding analytical solutions.*

$\varepsilon_{\rm sc}$		10^{-2} (L)	10^{-2} (Q)	10^{-3} (L)	10^{-3} (Q)	10^{-4} (Q)
$\langle N_{\rm sc} \rangle$	$(M = 200)$	2.74	2.11		2.34	3.31
	$(M = 1000)$	2.20	2.03	3.09	2.08	2.25

Table 3: *Average number $\langle N_{sc} \rangle$ of sub-cycles per time step. Influence of the stagnation tolerance ε_{sc}, the choice of initial guess and the number M of time steps.*

show that the quadratic guess consistently requires (on average) less sub-cycles that the linear guess, and that $\langle N_{\rm sc} \rangle$ remains close to 2 for all tested tolerances $\varepsilon_{\rm sc}$ when $M = 1000$ (small time step).

This example completes the validation of the proposed procedure by showing that the unknown motion of the submerged solid can be accurately recovered, and emphasizes the importance of using a good initial guess for the wet surface velocity in the sub-cycling.

5 Fluid-structure interaction between a stiffened hull and a gas bubble

Hull stiffening is of primary importance for a submarine to withstand the adverse effect of high hydrostatic pressures or underwater explosions while limiting its weight. This example accordingly considers the effects of a gas bubble created by an underwater explosion on a stiffened hull with representative characteristics and dimensions.

5.1 Geometry, modeling and discretization. The submerged structure is a cylindrical hull closed by two hemispheres, whose characteristics are given in Figure 9; the diameter and total length of the hull are $2a = 6.6$ m and $2L = 73.3$ m respectively. The internal side of the cylindrical part of the hull features 85 regularly spaced stiffeners, whose arrangement and dimensions (including thicknesses) are shown in Figure 10 (the hemispherical closing parts not being stiffened). The structure is made of steel with the following characteristics: mass density $\rho_s = 7800$ kg/m^3, Young's modulus $E = 204$ GPa, Poisson's ratio $\nu = 0.3$. The whole structural FE model is made of Abaqus ® shell elements (S4R), with 5 integration points along the thickness. The element sizes are such that the flange is meshed with two elements, the web with three elements, while six elements lie between two stiffeners for the cylindrical part (Fig. 10). This results in a FE model comprising approximately $3\,10^5$ nodes and 5 DOFs per node, with about 10^5 nodes located on the wet surface Γ.

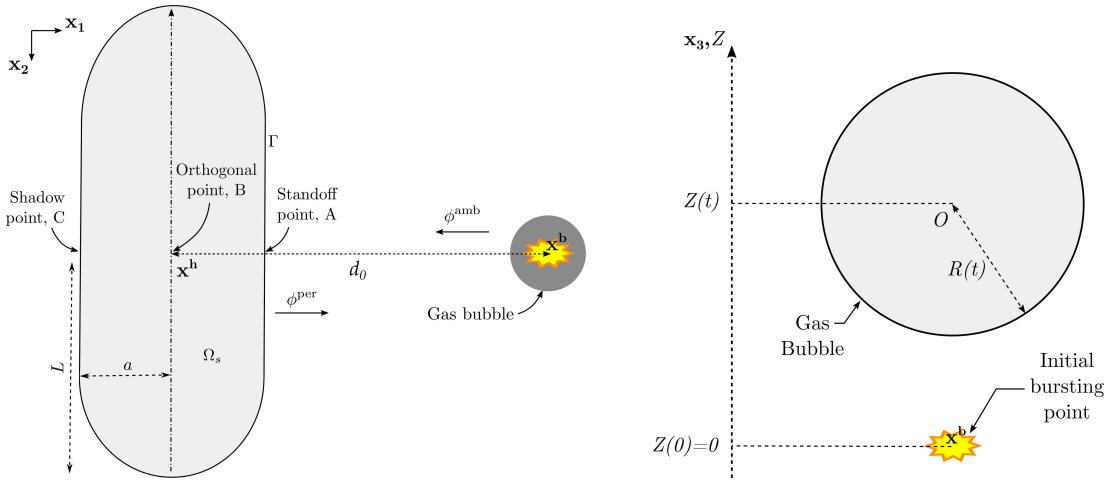

Figure 9: *FSI between the stiffened hull and the gas bubble, notations.*

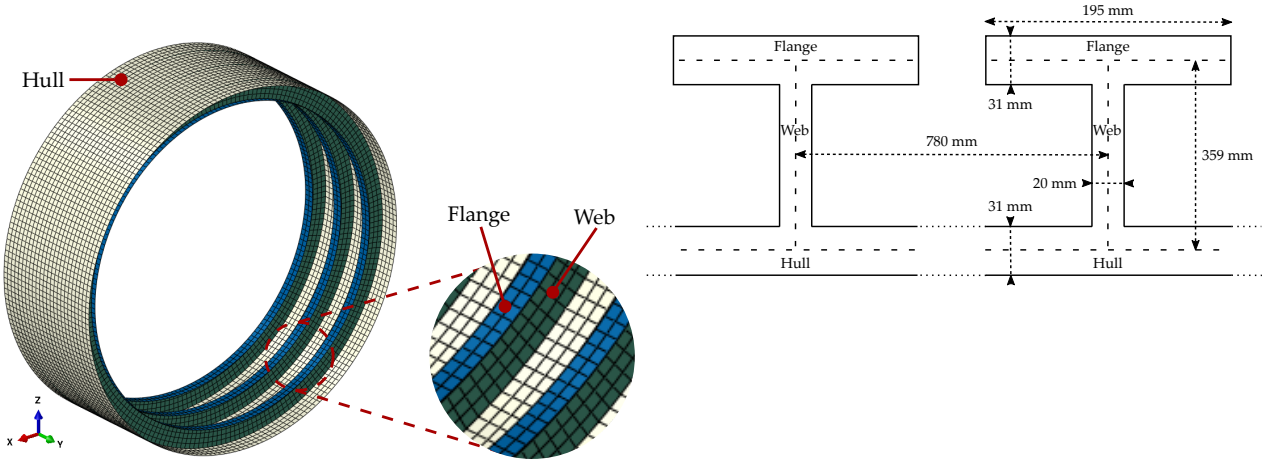

Figure 10: *Portion of the stiffened cylindrical hull: notations and terminology, stiffener shape and dimensions.*

The fluid region, made of water ($\rho_f = 1000$ kg/m^3, $c_f = 1500$ m/s), is taken as the entire infinite domain exterior to the wet surface. The implied assumption of a sufficiently remote water surface is reasonable since, for the considered time durations, the maximum variation of the bubble depth is about 15 m, which remains small compared to the initial depth of 100 m. The depth therefore manifests itself only through the hydrostatic part of the pressure in Bernoulli's equation and as a parameter of the bubble model given thereafter. The presented numerical results were obtained without taking into account the hydrostatic pressure.

5.2 Gas bubble model and characteristics. We consider an explosion of $\mathfrak{m} = 1000$ kg of TNT occurring at a point $\mathbf{x}^{\rm b}$ located at a distance $d_0 = 50$ m from the hull center $\mathbf{x}^{\rm h}$ (so the standoff distance is $d_s = d_0 - a = 46.7$ m), with $\mathbf{x}^{\rm b}$ and $\mathbf{x}^{\rm h}$ assumed to be at the same depth: $x_3^{\rm b} = x_3^{\rm h} = -100$ m (Fig. 9). The blast generates a gas bubble of maximum radius $R_{\max}^{\rm b}$ and pseudo-period $T^{\rm b}$ given by [32]

$$R_{\max}^{\rm b} = K_1 \Big(\frac{\rho g \mathfrak{m}}{p_0 - \rho g x_3^{\rm b}} \Big)^{1/3} \approx 7.3 \text{ m}, \qquad T^{\rm b} = K_2 \Big(\frac{\rho g \mathfrak{m}^{2/5}}{p_0 - \rho g x_3^{\rm b}} \Big)^{5/6} \approx 0.42 \text{ s} \tag{24}$$

(the dimensional constants having the values $K_1 \approx 3.50$ SI and $K_2 \approx 2.11$ SI [33]). The shock factor [10] $K := \sqrt{\mathfrak{m}}/d_s \simeq 0.68$ for this explosion is considered by practitioners to be quite large. As schematically depicted in Figure 2, the bubble generated by the explosion pulsates while its centre moves up towards the surface. Several models are available for describing the pulsating bubble motion; here we use the simple Hicks model, whereby the bubble is assumed to remain spherical (with a time-dependent radius $R(t)$) while moving vertically (with a time-dependent depth $x_3^{\rm b}(t) = x_3^{\rm b} + Z(t)$). The fluid motion outside the bubble and in the absence of a submerged structure predicted by this model is given by the ambient velocity potential

$$\phi^{\rm amb}(\mathbf{x}, t) = -\frac{R^2(t)\dot{R}(t)}{|\mathbf{x} - \mathbf{x}^{\rm b}(t)|} - \frac{R^3(t)\dot{Z}(t)(x_3 - x_3^{\rm b}(t))}{2|\mathbf{x} - \mathbf{x}^{\rm b}(t)|^3} \quad (|\mathbf{x} - \mathbf{x}^{\rm b}(t)| \geq R(t)), \tag{25}$$

where $\mathbf{x}^{\rm b}(t) = \mathbf{x}^{\rm b} + Z(t)\mathbf{e}_3$. From energy conservation arguments, the time-dependent parameters $R(t)$, $Z(t)$ of the above model are found by solving a system of two nonlinear ODEs, whose initial conditions are usually calibrated so that the response $t \mapsto (R(t), Z(t))$ is consistent with the maximum radius and pseudo-period (24) (see Chap.1 and App. C.2 of [26] for details). The resulting bubble radius and depth variations, for the explosion parameters as given above, are illustrated in Figure 11. The Hicks model

leads to a slightly smaller value of $R_{\max}$ than expected, and is also known to underestimate energy losses (compared to measured values), which manifests itself with a smaller than expected decline of $R_{\max}$ for each bubble expansion [23].

Comments on the bubble model. The adopted hypothesis of incompressible flow is suitable provided the characheristic time scale T_b of bubble motions is large enough compared to the characteristic time T_s of sound propagation phenomena. For this example or our target applications, the typical bubble pulsation period is $T_b \sim 0.5$ s, whereas typical distances (submarine length, distance between the bubble and the submarine) are $L \sim 100$ m, corresponding to a sound travel time of $T_s \sim 0.07$ s in water. Hence, $T_b \sim 15T_s$. This observation makes the incompressible flow hypothesis acceptable from an engineering standpoint, while indicating that high-accuracy modeling may require finer bubble models such as that proposed in [22] (which takes into account causal propagation effects and reduces to the Hicks model in the limiting case $T_s/T_b \to 0$). Such refined models can still be formulated in terms of an ambient potential ϕ^{amb}, but imply more complexity in the computational modeling of the fluid medium as ϕ^{amb} is no longer harmonic. A possible middle ground worthy of future investigation consists in still seeking a harmonic perturbed potential ϕ^{per} while using such non-harmonic ϕ^{amb} as input in the FSI problem (2)-(5).

The standoff distance $d_s = 46.7$ m is approximately 6 times the maximum bubble radius (24). Reducing the distance between the explosion and the structure could violate the hypotheses of remote underwater explosion, as the bubble dynamics should be computed taking into account the presence of the ship. For this reason, we consider an unrealistic explosive weight, to make the explosion severe enough without reducing the standoff distance.

5.3 Preliminary orders of magnitude. To estimate the magnitude of the main variables before performing the full FSI analysis, we begin by computing the fluid motion generated by the oscillating bubble when the submerged hull is rigid and motionless. We thus compute the velocity potential and pressure on the wet surface Γ over a duration of $T = 1$ s divided into $M = 1000$ time steps, by solving problem (27) with $\phi^{\text{amb}}(\mathbf{x}, t)$ given by (25) at each time instant. The wet surface Γ is meshed with three-noded linear triangular boundary elements comprising $N = 1890$ nodal fluid DOFs. Gravity and its effects (buoyant force, hydrostatic pressure) is disregarded for this preliminary evaluation.

The computed time histories of ϕ and p at the standoff point of the rigid hull are plotted in Figure 12. The perturbation ϕ^{per} of the velocity potential due to the hull is quite small compared to the ambient potential ϕ^{amb}. This is explained by the moderate spatial variation of ϕ^{amb} on Γ for the

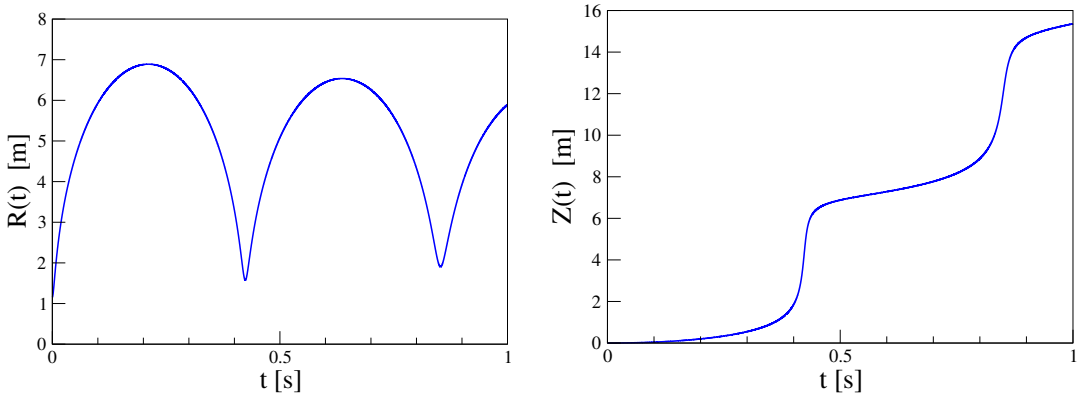

Figure 11: *Bubble radius and depth variation predicted by the Hicks model, for an underwater explosion of* 1000 *kg of TNT at water depth* $\xi_{exp} = 100$ *m.*

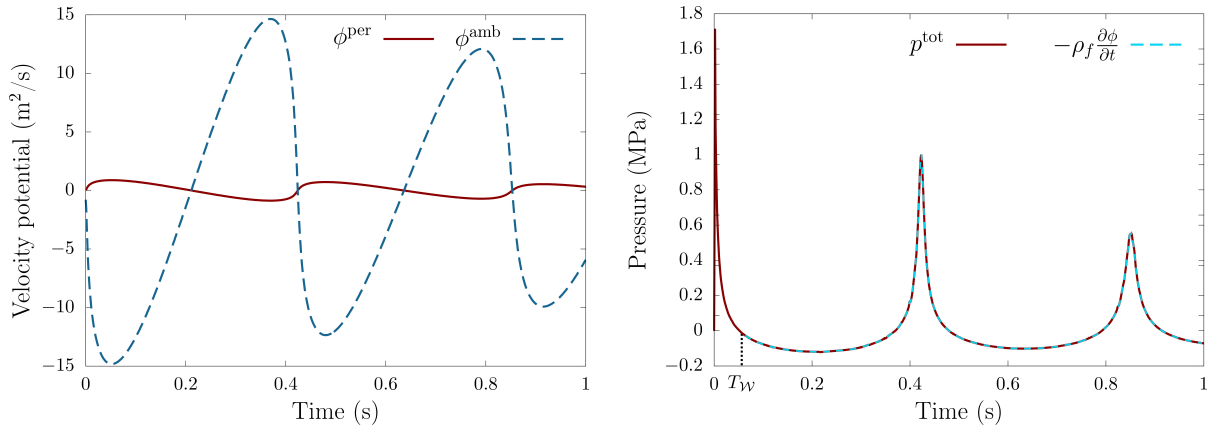

Figure 12: *Velocity potentials and total pressure at the standoff point of the rigid structure. The inertial contribution to the pressure for $t \geq T_{\mathcal{W}}$ is also shown.*

chosen considered location $\mathbf{x}^{\text{b}}(T)$ of the bubble center $\mathbf{x}^{\text{b}}(t)$; in fact, in the limiting case of an infinitely remote bubble for which ϕ^{amb} is constant on Γ, we have $\partial_{\mathbf{n}}\phi^{\text{amb}} = 0$ and therefore $\phi^{\text{per}} = 0$.

To reflect the fact that industrial applications of the bubble effect analysis would disregard its effect over a short initial duration $T_{\mathcal{W}}$ that is dominated by the initial shock wave, we shift the time origin in the bubble model (25) by setting the time variable therein to $t+T_{\mathcal{W}}$. Moreover, to avoid disrupting the FSI coupling algorithm by subjecting the structure to an artificial pressure jump at the first time step, we smoothly transition the pressure from a zero initial value to the bubble model pressure $p^{\text{b}}(t)$ over a short duration T_{smooth} by defining

$$p^{\text{b}}_{\eta}(t) := p^{\text{b}}(t+T_{\mathcal{W}})\,\eta\big(t/T_{\text{smooth}}\big), \qquad \eta(u) = \begin{cases} 0 & u \leq 0 \\ 1 - \exp\big(\frac{2e^{-1/u}}{u-1}\big), & 0 \leq u \leq 1 \\ 1 & u \geq 1. \end{cases},$$

where the above cutoff function η [1] is $C^{\infty}(\mathbb{R})$. All results shown thereafter use $T_{\mathcal{W}} = 50$ ms and $T_{\text{smooth}} = 10$ ms.

Figure 12 also shows the inertial contribution $-\rho_{\text{F}}\partial\phi/\partial t$ to the total pressure in Bernoulli's equation (3b), for $t \geq T_{\mathcal{W}}$. This inertial contribution is dominant, and remains largely so if the structure is deformable and mobile (the inertial contribution still constituting over 99 % of the pressure); this fact is well known in the naval industry [22, 23]. We nonetheless wanted to compute the pressure using Bernoulli's equation, rather than just its inertial approximation, to check and confirm its validity. Forgoing the evaluation of the approximated Bernoulli equation slightly speeds up the overall analysis, as $\nabla\phi$ no longer needs to be evaluated on Γ.

5.4 Numerical solution of the FSI problem. The FSI problem is treated by means of the procedure presented in Section 3.4: the fluid pressure is obtained from the ambient velocity potential (25) using Bernoulli's equation (3b), and provides the Neumann datum for the structure part, through (5). Notations and physical parameters are given in section 5.1.

Parameters. The wet surface is meshed with three-noded triangular boundary elements and features $N_f \approx 10^5$ DOFs for the fluid potential. The $\mathcal{H}$-matrix approximations of $\mathbf{H}_0$ and $\mathbf{G}_0$ are computed using a minimum block size $n_{\text{leaf}} = 200$ and a relative accuracy threshold equal to 10^{-4}, while the GMRES tolerance is set to 10^{-4}. Fields are interpolated from the BE mesh to the FE mesh, and *vice*

versa, using the code feflo.a [25]. The following time parameters are used: $T_{\mathcal{W}} = 50$ ms, $T_{\text{smooth}} = 10$ ms, analysis duration $T = 0.93$ s discretized into $M = 930$ time steps. The Hilber-Hughes-Taylor (HHT) implicit time stepping scheme, which is the default scheme of Abaqus ® implicit, is used for the structure, with $\alpha = 0.05$, $\beta = 0.275625$, $\gamma = 0.55$ [11, 15, 21]. The sub-cycling is performed with a constant initial guess for the velocity and $\varepsilon_{\text{sc}} = 10^{-2}$ (see Sec. 4.2), the structure being assumed to be at rest at the initial time $t = 0$. We allowed for the possibility of plasticity in the Abaqus ® model used, setting the elasticity limit to $\sigma_{\text{lim}} = 355$ MPa. However, as this study considers the effect of the bubble in isolation (i.e. leaving out the prior shock wave), the deformation was observed to remain elastic despite the high explosion charge.

Global deformation: bending. Figure 13 shows nine snapshots of the computed structure motion, taken every 100 ms. As expected, the most noticeable deformation mode is bending. This bending notably results from the dependence of the bubble ambient flow (25) on the distance to the bubble center: the cylinder extremities being farther to the bubble center than the cylinder center, the pressure magnitude is larger at the cylinder center. This effect gets more pronounced as the standoff distance reduces.

The structure undergoes a back-and-forth motion, induced by the bubble ebb and flow generating alternating positive and negative pressures (see Fig. 12). The stiffeners play a minor role in the bending process, and more generally in the structure response. Indeed, contrary to the shock wave case, the global deformation dominates the local ones. For that reason, some submarine hulls are equipped with longitudinal stiffeners (parallel to the cylinder axis) that improve the hull resistance to bending.

Convergence of sub-cycling iterations. For this example, the FSI iterative sub-cycling process, used at each time step, experienced convergence issues. To remedy them, we introduced a relaxation coefficient α, possibly depending on the iteration k, such that the Neumann data (6) for the $k+1$-th potential flow iterate is recast as

$$\partial_{\mathbf{n}}\phi_n^{k+1,\text{per}} = -\partial_{\mathbf{n}}\phi^{\text{amb}} + \alpha^k \mathbf{v}_n^k \cdot \mathbf{n} + (1-\alpha^k)\mathbf{v}_n^{k-1} \cdot \mathbf{n} \tag{26}$$

where $\mathbf{v}_n^k$ and $\mathbf{v}_n^{k-1}$ are structure velocity iterates. To obtain convergence, the relaxation parameter must be set to a low value. In this example, we set $\alpha = 0.1$, which allows the coupling iterations to converge, within $N_{sc} \sim 10$ sub-cycles for most time steps (those near the bubble pulses requiring $N_{sc} \sim 20$ sub-cycles). These values of N_{sc} make it potentially costly to refine either space or time discretizations. Moreover, the considered time and space discretisations yield displacements with smooth time variation, whereas the velocities become disturbed after the first bubble pulse. This in particular makes the linear or quadratic guesses of Sec. 4.2 for the velocities inefficient.

Computational work. The total computational cost for this FSI problem can be decomposed into three main contributions:

- the fluid BEM solutions;
- all other fluid computations related to post-processing: pressure evaluations using (3b), computation of the nodal forces from the nodal pressures, field interpolations using `feflo.a` ...
- the structure FEM solutions.

At the current stage of implementation, these components are not equally optimized. Most of our work to date has been devoted to the fluid BEM solves. Firstly, the $\mathcal{H}$-matrix representations of the integral operators are computed only once, at the first time step, which results in a drastic reduction of computational work since the cost of each subsequent matrix-vector product is small compared to this initial assembly time. Secondly, we use an efficient initial guess for our GMRES iterative solver

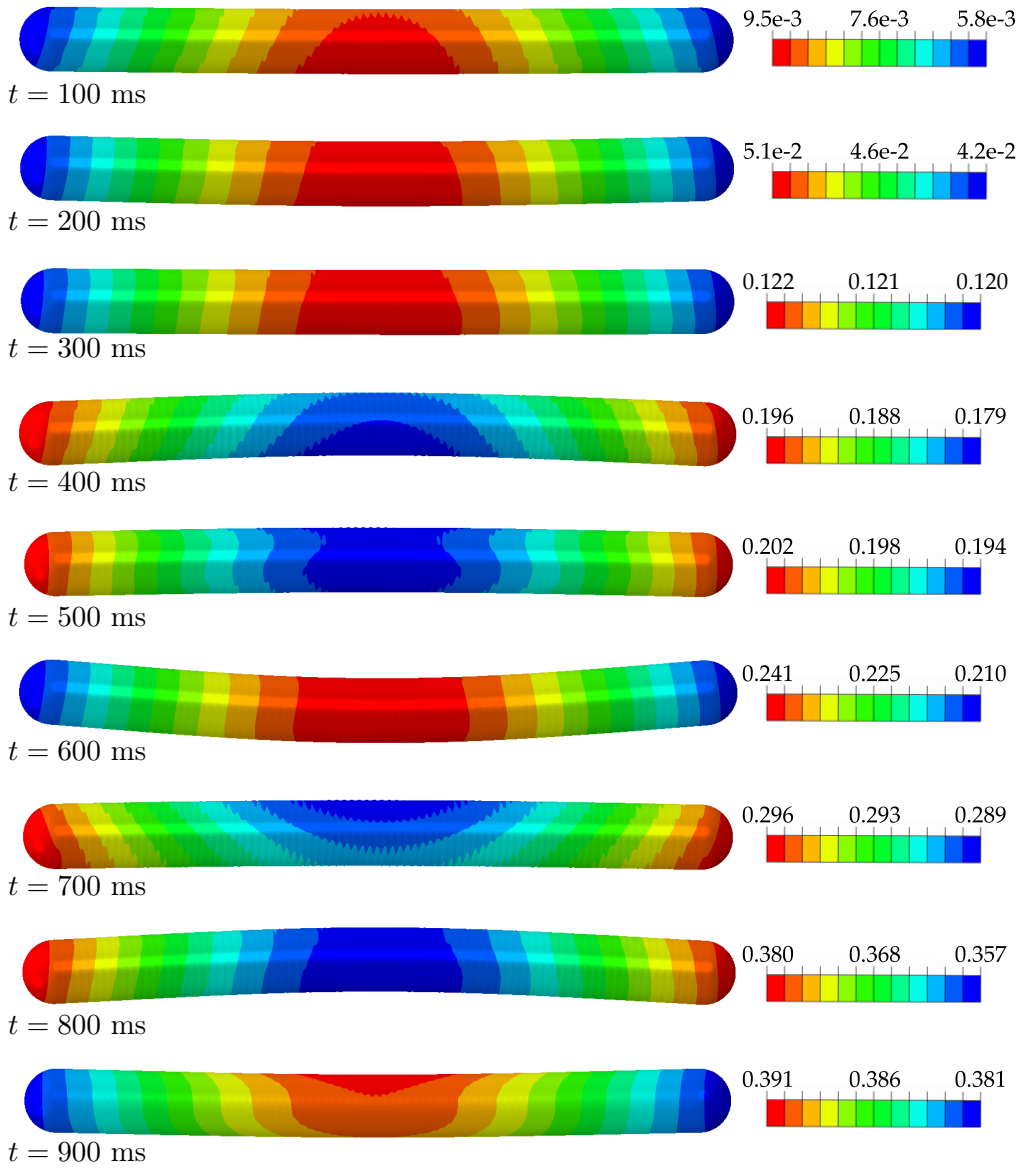

Figure 13: *Snapshots of the structure deformation (with a magnification factor of 70) during the FSI, for* $t \in [100, 900]$ *ms. The color maps show the 2-norm of the displacement vector on the wet surface.*

(the solution of the previous time step), resulting for this example in only about 5 GMRES iterations for each BEM solve. Finally, thanks to the $\mathcal{H}$-matrix method being embarrassingly parallel, the $\mathcal{H}$-matrix-vector product is parallelized on 36 CPUs. All these optimizations lead to a solution time of about 13 seconds per potential flow problem, and 10 seconds for all other fluid computations related to post-processing. This performance is satisfactory given the number $N_f \approx 10^5$ of fluid DOFs, for which standard BEMs would hardly have been usable. On the other hand, our computational environment did not provide us the same flexibility for optimizing the structure solution process, as increasing the number of CPUs also increases the number of Abaqus ® licences. We were thus prevented to fully exploit parallelization for them, and performed the Abaqus ® analyses on just 12 CPUs, for a cost of about 10 seconds per structure solution.

6 Concluding remarks

In this work, we have shown $\mathcal{H}$-matrix accelerated BEM to be a very efficient and appropriate method for solving coupled fluid-structure interaction problems, arising in the naval industry, where ships are subjected to pulsating potential flow motions, in particular thanks to the demonstrated reusability of integral operators in this context.

The computational performances of the coupled solution methodology can still be significantly improved, by minimizing the overall number of fluid and structure solutions needed for a given analysis with preserved accuracy. This objective can be met by reducing the number of sub-cycling iterations per time step and the overall number of time steps. Indeed, the simple alternating-solution sub-cycling method implemented here as a first try showed unsatisfactory convergence behavior when applied to a large-scale analysis, and we are currently investigating alternative algorithms whose convergence is both faster and guaranteed. Additionally, implementing variable time step strategies whereby refinement in time is selectively applied around instants where the bubble stops contracting and starts expanding again is also expected to yield substantial reductions in overall computational effort.

From a physical modeling viewpoint, it will also be necessary to include the effect of the free water surface or the sea bed in the analyses. As the Green's function for such configurations is not isotropic, the issue of BEM operator re-usability at each time step will require additional thinking.

References

[1] Anderson T.G., Bruno O.P., Lyon M. High-order, dispersionless "fast-hybrid" wave equation solver. Part I: O(1) sampling cost via incident-field windowing and recentering. *SIAM J. Sci. Comput.*, **42**:A1348–A1379 (2020).

[2] Arons A.B., Slifko J.P., Carter A. Secondary pressure pulses due to gas globe oscillation in underwater explosions. *J. Acoustical Society of America*, **20**:271–276 (1948).

[3] Banerjee P.K. *The boundary element methods in engineering*. McGraw-Hill, 2nd edn. (1994).

[4] Barras G., Souli M., Aquelet N., Couty N. Numerical simulation of underwater explosions using an ALE method. The pulsating bubble phenomena. *Ocean Engineering*, **41**:53–66 (2012).

[5] Bebendorf M. *Hierarchical matrices: a means to efficiently solve elliptic boundary value problems*, vol. 63 of *Lecture Notes in Computational Science and Engineering*. Springer (2008).

[6] Bebendorf M., Rjasanow S. Adaptive low-rank approximation of collocation matrices. *Computing*, **70**:1–24 (2003).

[7] Bonnet M. *Boundary integral equation methods in solids and fluids*. John Wiley & sons (1999).

[8] Chaillat S., Desiderio L., Ciarlet P. Theory and implementation of $\mathcal{H}$-matrix based iterative and direct solvers for Helmholtz and elastodynamic oscillatory kernels. *J. Comp. Phys.*, **351**:165–186 (2017).

[9] COFFEE. Accelerated BEM software, developed at POEMS laboratory. https://uma.ensta-paris.fr/soft/COFFEE/ (2020).

[10] Cole R.H. *Underwater explosions*. Princeton University Press (1948).

[11] Dassault Systèmes SIMULIA. Abaqus documentation, theory, analysis and user guides. https://abaqus-docs.mit.edu/2017/English/SIMACAEEXCRefMap/simaexc-c-docproc.htm (2017).

[12] Doinikov A.A. Translational motion of a spherical bubble in an acoustic standing wave of high intensity. *Physics of fluids*, **14**:1420–1425 (2002).

[13] Geers T.L., Hunter K.S. An integrated wave-effects model for an underwater explosion bubble. *J. Acoust. Soc. Am.*, **111**:1584–1601 (2002).

[14] Geers T.L., Park C.K. Optimization of the G&H bubble model. Published in *Shock and Vibration*, **12**:3–8 (2005).

[15] Géradin M., Rixen D. *Mechanical vibrations. Theory and application to structural dynamics*. Wiley (2015).

[16] Golub G., Van Loan C. *Matrix Computations*. The Johns Hopkins University Press, third edn. (1996).

[17] Graham D., Hobson J., Murphy P., Toole C., Cross S., Farnworth J. Efficient modelling of the structural response of submarine pressure hulls to underwater explosions. In *Warship 2017: Naval Submarines & UUVs, The Royal Institution of Naval Architects* (2017).

[18] Hackbusch W. A sparse matrix arithmetic based on H-matrix. Part I: Introduction to H-matrices. *Computing*, **62**:89–108 (1999).

[19] Henrot A., Pierre M. *Shape variation and optimization. A geometrical analysis.* European Mathematical Society (2018).

[20] Hicks A.N. Effect of bubble migration of explosion-induced whipping of ships. Tech. Rep. Washington, D.C., Naval Ship Research and Development Center (1970).

[21] Hughes T.J.R. *The finite element method: linear static and dynamic finite element analysis.* Prentice-Hall (1987).

[22] Hunter K.S., Geers T.L. Pressure and velocity fields produced by an underwater explosion. *J. Acoust. Soc. Am.*, **115**:1483–1496 (2004).

[23] Leblond C. *Modélisation de phénomènes fortement instationnaires en milieux couplés. Application au dimensionnement de structures immergées aux explosions sous-marines.* Ph.D. thesis, (French), Université de Nantes (2007).

[24] Liu Y., Zhang A., Tian Z., Wang S. Numerical investigation on global responses of surface ship subjected to underwater explosion in waves. *Ocean Engineering*, **161**:277–290 (2018).

[25] Loseille A. Chapter 10–Unstructured mesh generation and adaptation. In R. Abgrall, C.W. Shu (editors), *Handbook of numerical methods for hyperbolic problems*, vol. 18 of *Handbook of Numerical Analysis*, pages 263–302. Elsevier (2017).

[26] Mavaleix-Marchessoux D. *Modeling the fluid-structure interaction caused by a far-field underwater explosion.* Ph.D. thesis, Institut Polytechnique de Paris, https://tel.archives-ouvertes.fr/tel-03145479 (2020).

[27] Mavaleix-Marchessoux D., Bonnet M., Chaillat S., Leblé B. A fast BEM procedure using the Z-transform and high-frequency approximations for large-scale 3D transient wave problems. *Int. J. Numer. Meth. Engrg.*, **212**:4734–4767 (2020).

[28] Rokhlin V. Rapid solution of integral equations of classical potential theory. *Journal of computational physics*, **60**:187–207 (1985).

[29] Saad Y., Schultz M. GMRES: A generalized minimal residual algorithm for solving nonsymmetric linear systems. *SIAM J. Sci. Stat. Comput.*, **7**:856–869 (1986).

[30] Schotté J.S. *Influence de la gravité sur les vibrations linéaires d'une structure élastique contenant un liquide incompressible.* Ph.D. thesis, (French), Conservatoire National des Arts et Métiers, Paris, France (2001).

[31] Snay H.G. Hydrodynamics of underwater explosions. Published in *Symposium on Naval Hydrodynamics, National Academy of Sciences, Washington D.C.*, pages 325–346 (1956).

[32] Snay H.G. Underwater explosion phenomena: the parameters of migrating bubbles. Tech. rep., U. S. Naval Ordnance Laboratory, White Oak, Maryland (1962).

[33] Swisdak M.M. Explosion Effects and Properties. Part II. Explosion Effects in Water. Tech. Rep. NSWC/WOL TR 76–116, Naval Surface Weapons Center, Dahlgren, Virginia (1978).

[34] Véron E. *Calcul numérique des grandes déformations de structures minces en contact avec des fluides lourds.* Ph.D. thesis, (French), Université de Nantes (2016).

[35] Wang C., Khoo B. An indirect boundary element method for three-dimensional explosion bubbles. *Journal of Computational Physics*, **194**:451–480 (2004).

[36] Zhang A., Liu Y. Improved three-dimensional bubble dynamics model based on boundary element method. *Journal of Computational Physics*, **294**:208–223 (2015).

[37] Zhang A.M., Yao X.L. Interaction of underwater explosion bubble with complex elastic-plastic structure. *Appl. Math. Mech.*, **29**:89–100 (2008).

[38] Zong Z. A hydroplastic analysis of a free-free beam floating on water subjected to an underwater bubble. *Journal of Fluids and Structures*, **20**:359–372 (2005).

Appendix A Reference solutions for the motionless- and mobile-sphere problems

Motionless sphere. The fluid domain is $\Omega_{\rm F} := \{\mathbf{x} \in \mathbb{R}^3,\ |\mathbf{x}| > a\}$, see Figure 6. The perturbation $\phi^{\rm per}(\cdot,t) := \phi(\cdot,t) - \phi^{\rm amb}(\cdot,t)$ at time t of the flow induced by the presence of the sphere solves the exterior boundary-value problem

$$\Delta\phi^{\rm per} = 0 \ \text{ in } \Omega_{\rm S} \qquad \partial_{\mathbf{n}}\phi^{\rm per} = -\partial_{\mathbf{n}}\phi^{\rm amb} \ \text{ on } \Gamma \qquad \phi^{\rm per} \to 0 \ \text{ if } |\mathbf{x}| \to \infty \qquad (0 \le t \le T) \qquad (27)$$

with $\partial_{\mathbf{n}}\phi^{\text{amb}} = U(t)\,\mathbf{n}\cdot\mathbf{e}_1 = U(t)\,x_1/a$ as a consequence of (20). Problem (27) is easily solved in closed form for ϕ^{per} using separation of variables in spherical coordinates, whereupon ϕ is found as

$$\phi(\mathbf{x},t) = U(t)\Big(\frac{1}{2}\frac{a^3}{|\mathbf{x}|^3}+1\Big)x_1 \tag{28}$$

Then, using the above solution in Bernoulli's equation (3b) with its hydrostatic term set to zero, the pressure on Γ is readily obtained as

$$p(\mathbf{x},t) = C(t) - \frac{3\rho_{\text{F}}}{2}\dot{U}(t)x_1 + \frac{9\rho_{\text{F}}}{8a^2}U(t)^2(a^2-x_1^2) \qquad \mathbf{x}\in\Gamma$$

and the axial force result (21) finally follows from evaluating the integral with the above-given pressure (the value of $C(t)$ being irrelevant since $\int_\Gamma C(t)\mathbf{n}\,\mathrm{d}\Gamma = \mathbf{0}$).

Mobile sphere. The ambient flow still being uniaxial and uniform, the sphere has an axial translational displacement $\mathbf{d}(t) = d(t)\mathbf{e}_1$. Introducing coordinates $\mathbf{x}' := \mathbf{x}-d(t)\mathbf{e}_1$ following the sphere motion, the flow potential $\phi = \phi(\mathbf{x},t)$ can be expressed in terms of $\mathbf{x}'$ as $\phi(\mathbf{x},t) = \phi(\mathbf{x}+\mathbf{d}(t),t) =: \psi(\mathbf{x}',t)$. This change of unknown implies $\nabla\phi = \nabla'\psi$, $\Delta\phi = \Delta'\psi$ and $\partial_t\phi = \partial_t\psi - \dot{d}\partial_{x_1'}\psi$, with obvious notation. The flow perturbation caused by the moving sphere is therefore defined (in the moving coordinates) by the potential ψ^{per} solving problem (27) with $U(t)$ replaced by $U(t)-\dot{d}(t)$, and is thus given by (28) with the same substitution. As a result, the velocity potential for this problem is given by

$$\phi(\mathbf{x},t) = \psi(\mathbf{x}',t) = \big(U(t)-\dot{d}(t)\big)\Big(\frac{1}{2}\frac{a^3}{|\mathbf{x}'|^3}+1\Big)x_1' + \dot{d}(t)x_1' + U(t)d(t) \tag{29}$$

Bernoulli's equation (3b), with its hydrostatic term set again to zero, yields the pressure on Γ as

$$p(\mathbf{x},t) = C(t) + \frac{9\rho_{\text{F}}}{8a^2}\big(U(t)-\dot{d}(t)\big)^2\,(x_1'^2-a^2) + \frac{\rho_{\text{F}}}{2}\Big(\big(\ddot{d}(t)-3\dot{U}(t)\big)x_1' + \dot{d}^2(t) - 2(\dot{U}d+U\dot{d})(t)\Big),$$

and the corresponding axial net force, given by

$$f(t) = \frac{m_{\text{F}}}{2}\big(3\dot{U}(t)-\ddot{d}(t)\big), \tag{30}$$

(the value of $C(t)$ again not being relevant) features the two expected terms, namely the force in the absence of motion and the added mass term. The sphere moves according to Newton's second law, i.e.

$$(2m+m_{\text{F}})\ddot{d}(t) = 3mf(t), \tag{31}$$

from which the sphere motion (23) is easily obtained by using (30) in (31) and twice integrating in time. Finally, using (23) in (29) yields the flow solution in terms of $t\mapsto U(t)$, m, m_{F}, $d(0)$ and $\dot{d}(0)$.